Available online at www.sciencedirect.com

ScienceDirect

Journal of Magnesium and Alloys 10 (2022) 129–145

www.elsevier.com/locate/jma

Full Length Article

Effect of carrier gases on the entrainment defects within AZ91 alloy castings

Tian Li[a,b], J.M.T. Davies[a], Xiangzhen Zhu[c,*]

[a] University of Birmingham, Birmingham B15 2TT, United Kingdom
[b] Grainger and Worrall Ltd, Bridgnorth WV15 5HP, United Kingdom
[c] Brunel Centre for Advanced Solidification Technology, Brunel University London, Kingston Ln, London, Uxbridge UB8 3PH, United Kingdom

Received 13 March 2021; received in revised form 15 June 2021; accepted 5 July 2021
Available online 4 August 2021

Abstract

An entrainment defect (also known as a double oxide film defect or bifilm) acts a void containing an entrapped gas when submerged into a light-alloy melt, thus reducing the quality and reproducibility of the final castings. Previous publications, carried out with Al-alloy castings, reported that this trapped gas could be subsequently consumed by the reaction with the surrounding melt, thus reducing the void volume and negative effect of entrainment defects. Compared with Al-alloys, the entrapped gas within Mg-alloy might be more efficiently consumed due to the relatively high reactivity of magnesium. However, research into the entrainment defects within Mg alloys has been significantly limited. In the present work, AZ91 alloy castings were produced under different carrier gas atmospheres (i.e., SF_6/CO_2, SF_6/air). The evolution processes of the entrainment defects contained in AZ91 alloy were suggested according to the microstructure inspections and thermodynamic calculations. The defects formed in the different atmospheres have a similar sandwich-like structure, but their oxide films contained different combinations of compounds. The use of carrier gases, which were associated with different entrained-gas consumption rates, affected the reproducibility of AZ91 castings.

© 2021 Chongqing University. Publishing services provided by Elsevier B.V. on behalf of KeAi Communications Co. Ltd.
This is an open access article under the CC BY-NC-ND license (http://creativecommons.org/licenses/by-nc-nd/4.0/)
Peer review under responsibility of Chongqing University

Keywords: Magnesium alloy; Casting; Oxide film, Bifilm, Entrainment defect, Reproducibility.

1. Introduction

As the lightest structural metal available on Earth, magnesium became one of the most attractive light metals over the last few decades. The magnesium industry has consequently experienced a rapid development in the last 20 years [1,2], indicating a large growth in demand for Mg alloys all over the world. Nowadays, the use of Mg alloys can be found in the fields of automobiles, aerospace, electronics and etc.[3,4]. It has been predicted that the global consumption of Mg metals will further increase in the future, especially in the automotive industry, as the energy efficiency requirement of both traditional and electric vehicles further push manufactures lightweight their design [3,5,6].

The sustained growth in demand for Mg alloys motivated a wide interest in the improvement of the quality and mechanical properties of Mg-alloy castings. During a Mg-alloy casting process, surface turbulence of the melt can lead to the entrapment of a doubled-over surface film containing a small quantity of the surrounding atmosphere, thus forming an entrainment defect (also known as a double oxide film defect or bifilm) [7–10]. The random size, quantity, orientation, and placement of entrainment defects are widely accepted to be significant factors linked to the variation of casting properties [7]. In addition, Peng et al. [11] found that entrained oxides films in AZ91 alloy melt acted as filters to Al_8Mn_5 particles, trapping them as they settle. Mackie et al. [12] further suggested that entrained oxide films can act to trawl the intermetallic particles, causing them to cluster and form extremely

* Corresponding author.
E-mail addresses: TLi@gwcast.com (T. Li), jdavies@physics.org (J.M.T. Davies), xiangzhen.zhu@brunel.ac.uk (X. Zhu).

https://doi.org/10.1016/j.jma.2021.07.005
2213-9567/© 2021 Chongqing University. Publishing services provided by Elsevier B.V. on behalf of KeAi Communications Co. Ltd. This is an open access article under the CC BY-NC-ND license (http://creativecommons.org/licenses/by-nc-nd/4.0/) Peer review under responsibility of Chongqing University

large defects. The clustering of intermetallic compounds made the entrainment defects more detrimental for the casting properties.

Most of the previous studies regarding entrainment defects were carried out on Al-alloys [7,13–18], and a few potential methods have been suggested for diminishing their negative effect on the quality of Al-alloy castings. Nyahumwa et al.,[16] shows that the void volume within entrainment defects could be reduced by a hot isostatic pressing (HIP) process. Campbell [7] suggested the entrained gas within the defects could be consumed due to reaction with the surrounding melt, which was further verified by Raiszedeh and Griffiths [19].The effect of the entrained gas consumption on the mechanical properties of Al-alloy castings has been investigated by [8,9], suggesting that the consumption of the entrained gas promoted the improvement of the casting reproducibility.

Compared with the investigation concerning the defects within Al-alloys, research into the entrainment defects within Mg-alloys has been significantly limited. The existence of entrainment defects has been demonstrated in Mg-alloy castings [20,21], but their behaviour, evolution, as well as entrained gas consumption are still not clear.

In a Mg-alloy casting process, the melt is usually protected by a cover gas to avoid magnesium ignition. The cavities of sand or investment moulds are accordingly required to be flushed with the cover gas prior to the melt pouring [22]. Therefore, the entrained gas within Mg-alloy castings should contain the cover gas used in the casting process, rather than air only, which may complicate the structure and evolution of the corresponding entrainment defects.

SF_6 is a typical cover gas widely used for Mg-alloy casting processes [23–25]. Although this cover gas has been restricted to use in European Mg-alloy foundries, a commercial report has pointed out that this cover is still popular in global Mg-alloy industry, especially in the countries which dominated the global Mg-alloy production, such as China, Brazil, India, etc. [26]. In addition, a survey in academic publications also showed that this cover gas was widely used in recent Mg-alloy studies [27]. The protective mechanism of SF_6 cover gas (i.e., the reaction between liquid Mg-alloy and SF_6 cover gas) has been investigated by several previous researchers, but the formation process of the surface oxide film is still not clearly understood, and even some published results are conflicting with each other. In early 1970s, Fruehling [28] found that the surface film formed under SF_6 was MgO mainly with traces of fluorides, and suggested that SF_6 was absorbed in the Mg-alloy surface film. Couling [29] further noticed that the absorbed SF_6 reacted with the Mg-alloy melt to form MgF_2. In last 20 years, different structures of the Mg-alloy surface films have been reported, as detailed below.

(1) *Single-layered film*. Cashion [30,31] used X-ray Photoelectron Spectroscopy (XPS) and Auger Spectroscopy (AES) to identify the surface film as MgO and MgF_2. He also found that composition of the film was constant throughout the thickness and the whole experimental holding time. The film observed by Cashion had a single-layered structure created from a holding time from 10 min to 100 min.

(2) *Double-layered film*. Aarstad et. al [32] reported a doubled-layered surface oxide film in 2003. They observed several well-distributed MgF_2 particles attached to the preliminary MgO film and grew until they covered 25–50% of the total surface area. The inward diffusion of F through the outer MgO film was the driving force for the evolution process. This double-layered structure was also supported by Xiong's group [25,33] and Shih et al. [34].

(3) *Triple-layered film*. The triple-layered film and its evolution process were reported in 2002 by Pettersen [35]. Pettersen found that the initial surface film was a MgO phase and then gradually evolved to the stable MgF_2 phase by the inward diffusion of F. In the final stage, the film has a triple-layered structure with a thin O-rich interlayer between the thick top and bottom MgF_2 layers.

(4) *Oxide film consisted of discrete particles*. Wang et al [36] stirred the Mg-alloy surface film into the melt under a SF_6 cover gas, and then inspect the entrained surface film after the solidification. They found that the entrained surface films were not continues as the protective surface films reported by other researchers but composed of discrete particles. The young oxide film was composed of MgO nano-sized oxide particles, while the old oxide films consist of coarse particles (about 1 μm in average size) on one side that contained fluorides and nitrides.

The oxide films of a Mg-alloy melt surface or an entrained gas are both formed due to the reaction between liquid Mg-alloy and the cover gas, thus the above-mentioned research regarding the Mg-alloy surface film gives valuable insights into the evolution of entrainment defects. The protective mechanism of SF_6 cover gas (i.e., formation of a Mg-alloy surface film) therefore indicated a potential complicated evolution process of the corresponding entrainment defects.

However, it should be noted that the formation of a surface film on a Mg-alloy melt is in a different situation to the consumption of an entrained gas that is submerged into the melt. For example, a sufficient amount of cover gas was supported during the surface film formation in the studies previously mentioned, which suppressed the depletion of the cover gas. In contrast, the amount of entrained gas within a Mg-alloy melt is finite, and the entrained gas may become fully depleted. Mirak [37] introduced 3.5%SF_6/air bubbles into a pure Mg-alloy melt solidifying in a specially designed permanent mould. It was found that the gas bubbles were entirely consumed, and the corresponding oxide film was a mixture of MgO and MgF_2. However, the nucleation sites (such as the MgF_2 spots observed by Aarstad [32] and Xiong [25,33]) were not observed. Mirak also speculated that the MgF_2 formed prior to MgO in the oxide film based on the composition analysis, which was opposite to the surface film formation process reported in previous literatures (i.e., MgO

Table 1
Composition (wt.%) of the AZ91 alloy used in this study.

Al	Zn	Mn	Si	Fe	Ni	Mg
9.4	0.61	0.15	0.02	0.005	0.0017	Residual

formed prior to MgF_2). Mirak's work indicated that the oxide-film formation of an entrained gas may be quite different from that of surface films, but he did not reveal the structure and evolution of the oxide films.

In addition, the use of carrier gas in the cover gases also influenced the reaction between the cover gas and the liquid Mg-alloy. SF_6/air required a higher content of SF_6 than did a SF_6/CO_2 carrier gas [38], to avoid the ignition of molten magnesium, revealing different gas-consumption rates. Liang et.al [39] suggested that carbon was formed in the surface film when CO_2 was used as a carrier gas, which was different from the films formed in SF_6/air. An investigation into Mg combustion [40] reported a detection of Mg_2C_3 in the Mg-alloy sample after burning in CO_2, which not only supported Liang's results, but also indicated a potential formation of Mg carbides in double oxide film defects.

The work reported here is an investigation into the behaviour and evolution of entrainment defects formed in AZ91 Mg-alloy castings, protected by different cover gases (i.e., SF_6/air and SF_6/CO_2). These carrier gases have different protectability for liquid Mg alloy, which may be therefore associated with different consumption rates and evolution processes of the corresponding entrained gases. The effect of the entrained-gas consumption on the reproducibility of AZ91 castings was also studied.

2. Experiment

2.1. Melting and casting

Three kilograms AZ91 alloy was melted in a mild steel crucible at 700 ± 5 °C. The composition of the AZ91 alloy has been shown in Table 1. Prior to heating, all oxide scale on the ingot surface was removed by machining. The cover gases used were 0.5%SF_6/air or 0.5%SF_6/CO_2 (vol.%) at a flow rate of 6 L/min for different castings. The melt was degassed by argon with a flow rate of 0.3 L/min for 15 min [41,42], and then poured into sand moulds. Prior to pouring, the sand mould cavity was flushed with the cover gas for 20 min [22]. The residual melt (around 1 kg) was solidified in the crucible.

Fig. 1(a) shows the dimensions of the casting with runners. A top-filling system was deliberately used to generate entrainment defects in the final castings. Green and Campbell [7,43] suggested that a top-filling system caused more entrainment events (i.e., bifilms) during a casting process, compared with a bottom-filling system. A melt flow simulation (Flow-3D software) of this mould, using Reilly's model [44] regarding the entrainment events, also predicted that a large amount of bifilms would be contained in the final casting (denoted by the black particles in Fig. 1b).

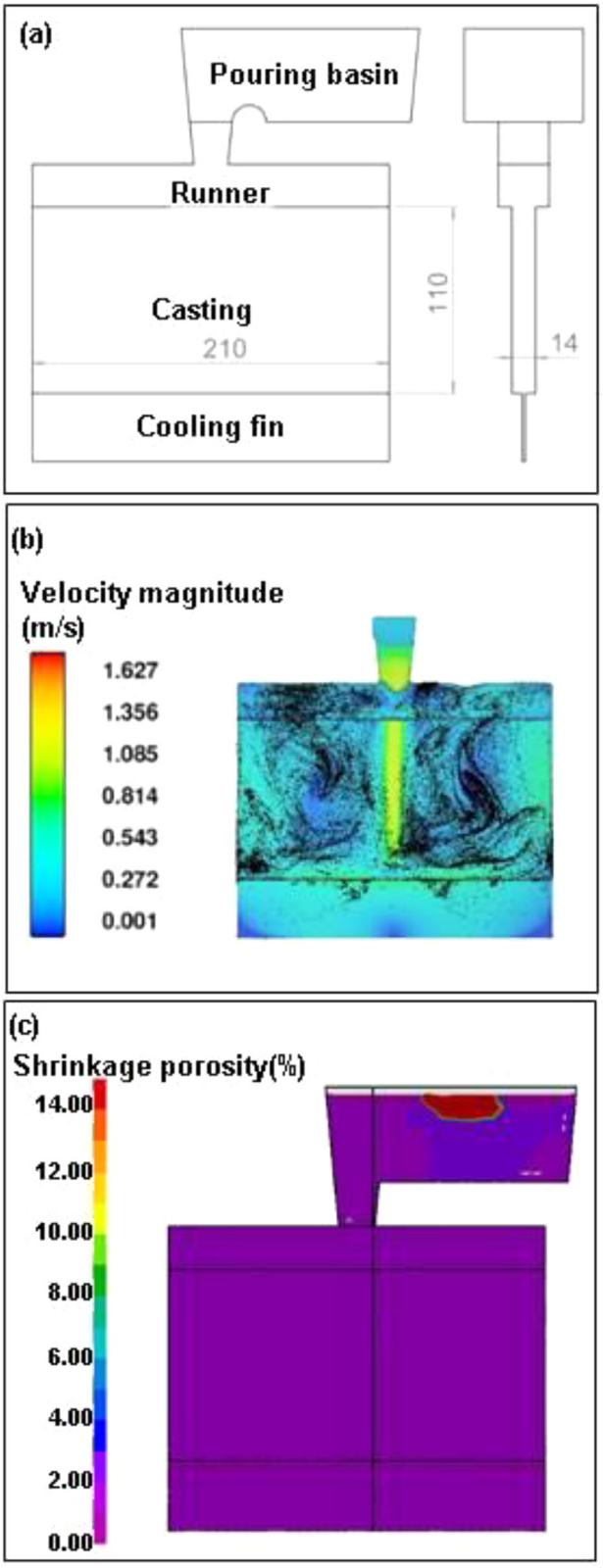

Fig. 1. (a) Dimensions of the casting with runners (unit: mm), (b) a melt flow simulation using Flow-3D software together with Reilly's model[44], predicted that a large amount of bifilms (denoted by the black particles) would be contained in the final casting. (c) A solidification simulation using Pro-cast software showed that no shrinkage defect was contained in the final casting.

Shrinkage defects also affect the mechanical properties and reproducibility of castings. Since this study focused on the effect of bifilms on the casting quality, the mould has been deliberately designed to avoid generating shrinkage defects. A solidification simulation using ProCAST software showed that no shrinkage defect would be contained in the final casting, as shown in Fig. 1c. The casting soundness has also been confirmed using a real time X-ray prior to the test bar machining.

The sand moulds were made from resin-bonded silica sand, containing 1wt. % PEPSET 5230 resin and 1wt. % PEPSET 5112 catalyst. The sand also contained 2 wt.% Na_2SiF_6 to act as an inhibitor [45]. The pouring temperature was 700 ± 5 °C. After the solidification, a section of the runner bars was sent to the Sci-Lab Analytical Ltd for a H-content analysis (LECO analysis), and all the H-content measurements were carried out on the 5th day after the casting process. Each of the castings was machined into 40 test bars for a tensile strength test, using a Zwick 1484 tensile test machine with a clip extensometer. The fracture surfaces of the broken test bars were examined using Scanning Electron Microscope (SEM, Philips JEOL7000) with an accelerating voltage of 5–15 kV. The fractured test bars, residual Mg-alloy solidified in the crucible, and the casting runners were then sectioned, polished and also inspected using the same SEM. The cross-section of the oxide film found on the test-bar fracture surface was exposed by the Focused Ion Beam milling technique (FIB), using a CFEI Quanta 3D FEG FIB-SEM. The oxide film required to be analysed was coated with a platinum layer. Then, a gallium ion beam, accelerated to 30 kV, milled the material substrate surrounding the platinum coated area to expose the cross section of the oxide film. EDS analysis of the oxide film's cross section was carried out using the FIB equipment at accelerating voltage of 30 kV.

2.2. Oxidation cell

As previously mentioned, several past researchers investigated the protective film formed on a Mg-alloy melt surface [38,39,46–52]. During these experiments, the amount of cover gas used was sufficient, thus suppressing the depletion of fluorides in the cover gas. The experiment described in this section used a sealed oxidation cell, which limited the supply of cover gas, to study the evolution of the oxide films of entrainment defects. The cover gas contained in the oxidation cell was regarded as large-size "entrained bubble".

As shown in Fig. 2, the main body of the oxidation cell was a closed-end mild steel tube which had an inner length of 400 mm, and an inner diameter of 32 mm. A water-cooled copper tube was wrapped around the upper section of the cell. When the tube was heated, the cooling system created a temperature difference between the upper and lower sections, causing the interior gas to convect within the tube. The temperature was monitored by a type-K thermocouple located at the top of the crucible. Nie et al. [53] suggested that the SF_6 cover gas would react with the steel wall of the holding furnace when they investigated the surface film of a Mg-alloy

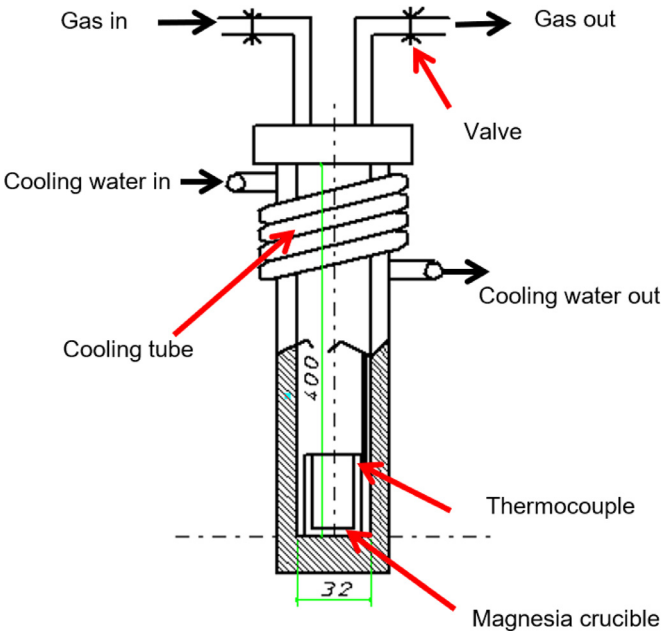

Fig. 2. Schematic of the oxidation cell used to study the evolution of the oxide films of the entrainment defects (unit mm).

melt. To avoid this reaction, the interior surface of the steel oxidation cell (shown in Fig. 2) and the upper half section of the thermocouple were coated with boron nitride (the Mg-alloy was not in contact with boron nitride).

During the experiment, a block of solid AZ91 alloy was placed in a magnesia crucible located at the bottom of the oxidation cell. The cell was heated to 100 °C in an electric resistance furnace under a gas flow rate of 1 L/min. The cell was held at this temperature for 20 min, to replace the original trapped atmosphere (i.e. air). Then, the oxidation cell was further heated to 700 °C, melting the AZ91 sample. The gas inlet and exit valves were then closed, creating a sealed environment for oxidation under a limited supply of cover gas. The oxidation cell was then held at 700 ± 10 °C for periods of time from 5 min to 30 min in 5-min intervals. At the end of each holding time, the cell was quenched in water. After cooling to room temperature, the oxidised sample was sectioned, polished, and subsequently examined by SEM.

3. Results

3.1. Structure and composition of the entrainment defects formed in SF_6/air

The structure and composition of the entrainment defect formed in the AZ91 castings under a cover gas of 0.5%SF_6/air was observed by SEM and EDS. The results indicate that there exist two types of entrainment defects which are sketched in Fig. 3: (1) Type A defect whose oxide film has a traditional single-layered structure and (2) Type B defect, whose oxide film has two layers. The details of these defects were introduced in the following. Here it should be noticed that, as the entrainment defects are also known as biofilms

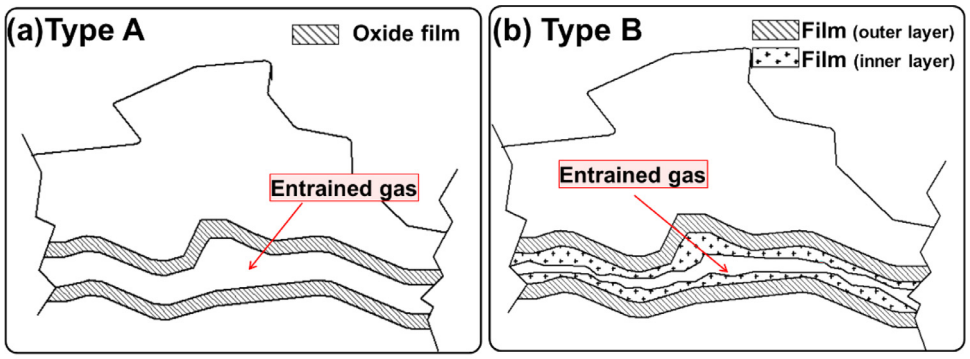

Fig. 3. Schematic of the different types of entrainment defects found in AZ91 castings. (a) Type A defect with a single-layered oxide film and (b) Type B defect with two-layered oxide film.

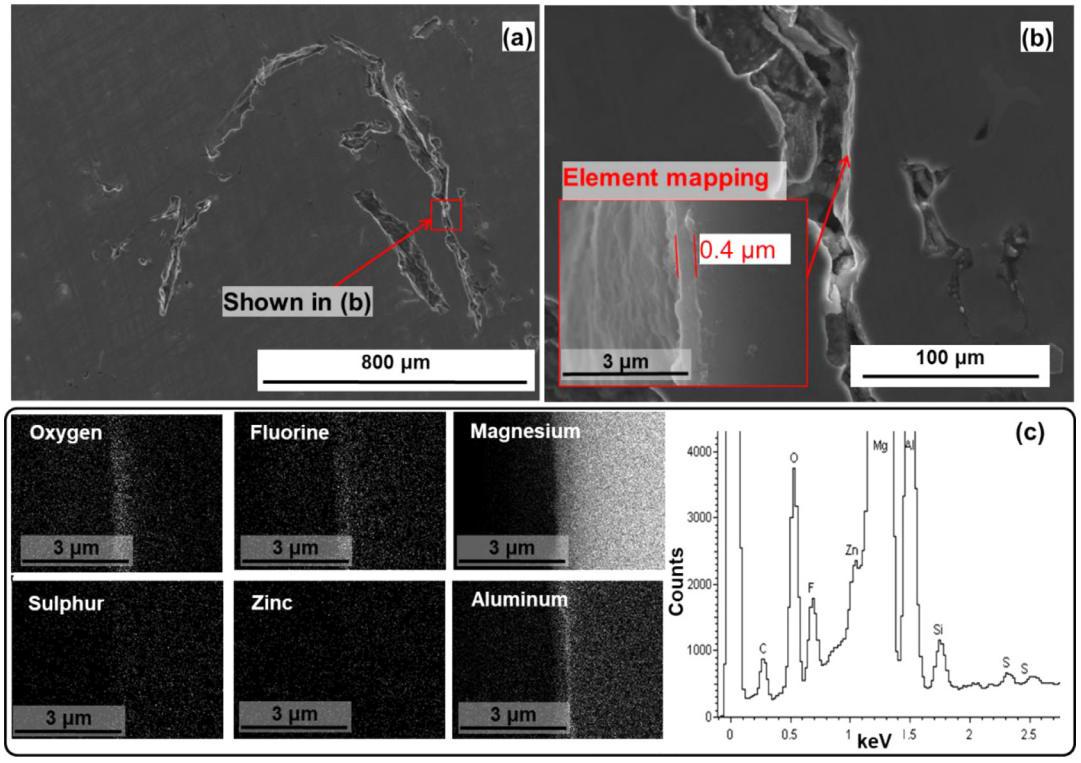

Fig. 4. (a) A Type A entrainment defect formed in SF_6/air and having a single-layered oxide film, (b) the oxide film of this defect, (c) SEM-EDS element maps (using Philips JEOL7000) corresponding to the area highlighted in (b).

or double oxide film, the oxide films of Type B defect were referred to as "multi-layered oxide film" or "multi-layered structure" in the present work to avoid a confusing description such as "the double-layered oxide film of a double oxide film defect".

Fig. 4(a-b) shows a Type A defect having a compact single-layered oxide film with about 0.4 μm thickness. Oxygen, fluorine, magnesium and aluminium were detected in this film (Fig. 4c). It is speculated that oxide film is the mixture of fluoride and oxide of magnesium and aluminium. The detection of fluorine revealed that an entrained cover gas was contained in the formation of this defect. That is to say that the pores shown in Fig. 4(a) were not shrinkage defects or hydrogen porosity, but entrainment defects. The detection of aluminium was different with Xiong and Wang's previous study [47,48], which showed that no aluminium was contained in their surface film of an AZ91 melt protected by a SF_6 cover gas. Sulphur could not be clearly recognized in the element map, but there was a S-peak in the corresponding ESD spectrum.

Fig. 5(a-b) shows a Type B entrainment defect having a multi-layered oxide film. The compact outer layers of the oxide films were enriched with fluorine and oxygen (Fig. 5c), while their relatively porous inner layers were only enriched

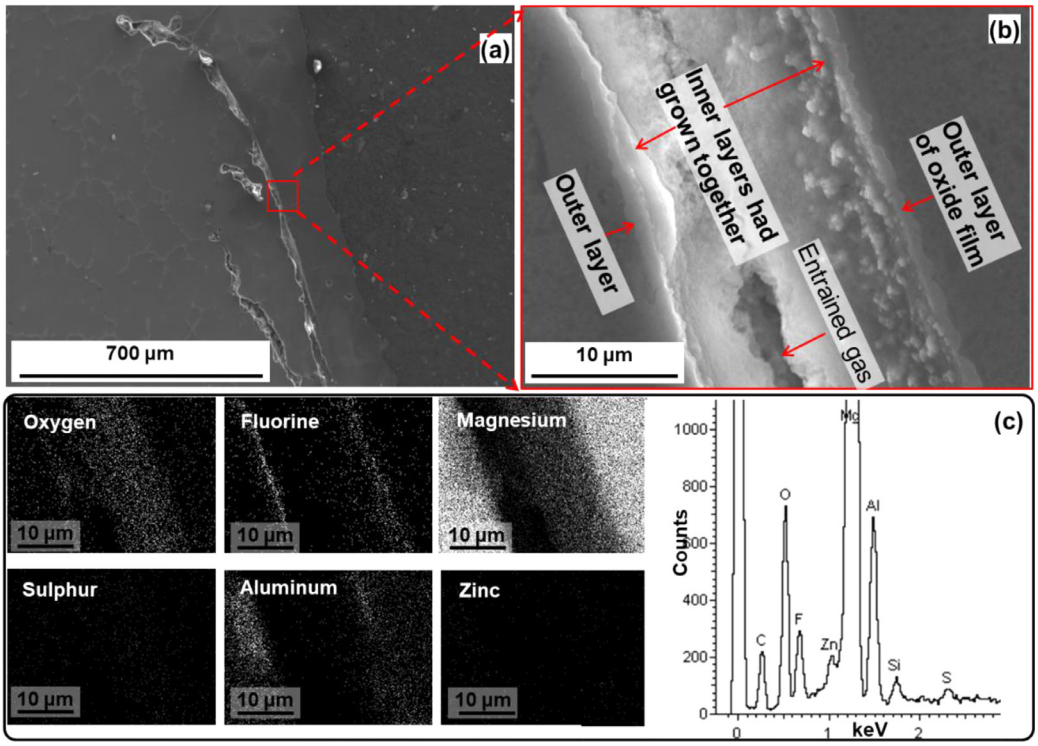

Fig. 5. (a) A Type B entrainment defect formed in SF6/air and having a multi-layered oxide film, (b) the oxide films of this defect have grown together, (c) SEM-EDS element maps (using Philips JEOL7000) corresponding to the area shown in (b).

with oxygen (i.e., poor in fluorine) and partly grew together, thus forming a sandwich-like structure. Therefore, it is speculated that the outer layer is the mixture of fluoride and oxide, while the inner layer is mainly oxide. Sulphur could only be recognized in the EDX spectrum and could not be clearly identified in the element map, which might be due to the small S-content in the cover gas (i.e., 0.5% volume content of SF_6 in the cover gas). In this oxide film, aluminium was contained in the outer layer of this oxide film but could not be clearly detected in the inner layer. Moreover, the distribution of Al seems to be uneven. It can be found that, in the right side of the defect, aluminium exists in the film but its concentration can not be identified to be higher than the matrix. However, there is a small area with much higher aluminium concentration in the left side of the defect. Such an uneven distribution of aluminium was also observed in other defects (shown in the following), and it is the result of the formation of some oxide particles in or under the film.

Figs. 4 and 5 show cross sectional observations of the entrainment defects formed in the AZ91 alloy sample cast under a cover gas of SF_6/air. It is not sufficient to characterize the entrainment defects only by the figures observed from the two-dimensional section. To have a further understanding, the surface of the entrainment defects (i.e. the oxide film) was further studied by observing the fracture surface of the test bars.

Fig. 6(a) shows fracture surfaces of an AZ91 alloy tensile test bar produced in SF_6/air. Symmetrical dark regions can be seen on both sides of the fracture surfaces. Fig. 6(b) shows boundaries between the dark and bright regions. The bright region consisted of jagged and broken features, while the surface of the dark region was relatively smooth and flat. In addition, the EDS results (Fig. 6c-d and Table 2) show that fluorine, oxygen, sulphur, and nitrogen were only detected in the dark regions, indicating that the dark regions were surface protective films entrained into the melt. Therefore, it could be suggested that the dark regions were an entrainment defect with consideration of their symmetrical nature. Similar defects on fracture surfaces of Al-alloy castings have been previously reported [7]. Nitrides were only found in the oxide films on the test-bar fracture surfaces but never detected in the cross-sectional samples shown in Figs. 4 and 5. An underlying reason is that the nitrides contained in these samples may have hydrolysed during the sample polishing process [54].

Table 2
EDS results (wt.%) corresponding to the regions shown in Fig. 6 (cover gas: SF_6/air).

	C	O	Mg	F	Al	Zn	S	N
Dark region in Fig. 6(b)	3.48	1.32	79.13	0.47	13.63	0.57	0.08	0.73
Bright region in Fig. 6(b)	3.58	-	84.48	-	11.25	0.68	–	–

In conjunction with the cross-sectional observation of the defects shown in Figs. 4 and 5, the structure of an entrainment defect contained in a tensile test bar was sketched as shown in Fig. 6(e). The defect contained an entrained gas enclosed by its oxide film, creating a void section inside the test bar.

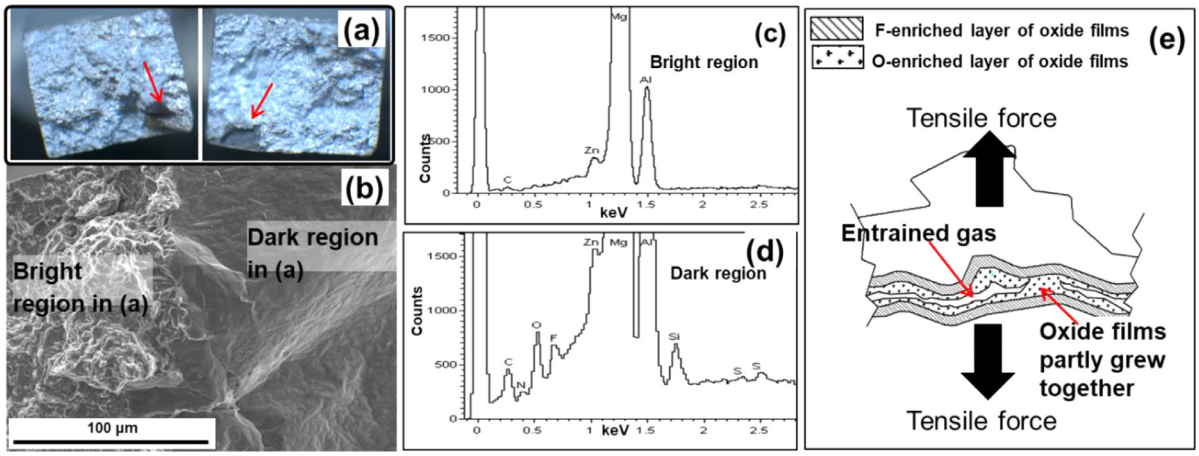

Fig. 6. (a) A pair of the fracture surfaces of a AZ91 alloy tensile test bar produced under a cover gas of SF_6/air. The dimension of the fracture surface is 5 mm × 6 mm, (b) a section of the boundary between the dark and bright regions shown in (a), (c-d) EDS spectrum of the (c) bright regions and (d) dark regions, (e) schematic of an entrainment defect contained in a test bar.

When the tensile force applied on the defect during the fracture process, the crack was initiated at the void section and propagated along the entrainment defect, since cracks would be propagated along the weakest path [55]. Therefore, when the test bar was finally fractured, the oxide films of entrainment defect appeared on both fracture surfaces of the test bar, as shown in Fig. 6(a).

3.2. Structure and composition of the entrainment defects formed in SF_6/CO_2

Similar to the entrainment defect formed in SF_6/air, the defects formed under a cover gas of 0.5%SF_6/CO_2 also had two types of oxide films (i.e., single-layered and multi-layered types). Fig. 7(a) shows an example of the entrainment defects containing a multi-layered oxide film. A magnified observation to the defect (Fig. 7b) shows that the inner layers of the oxide films had grown together, presenting a sandwich-like structure, which was similar to the defects formed in an atmosphere of SF_6/air (Fig. 5b). An EDS spectrum (Fig. 7c) revealed that the joint area (inner layer) of this sandwich-like structure mainly contained magnesium oxides. Peaks of fluorine, sulphur, and aluminium were recognized in this EDS spectrum, but their amount was relatively small. In contrast, the outer layers of the oxide films were compact and composed of a mixture of fluorides and oxides (Fig. 7d-e).

Fig. 8(a) shows an entrainment defect on the fracture surfaces of an AZ91 alloy tensile test bar, which was produced in an atmosphere of 0.5%SF_6/CO_2. The corresponding EDS results (Table 3) showed that oxide film contained fluorides and oxides. Sulphur and nitrogen were not detected. Besides, a magnified observation (Fig. 8b) indicated spots on the oxide film surface. The diameter of the spots ranged from hundreds of nanometres to a few micron meters.

To further reveal the structure and composition of the oxide film clearly, the cross-section of the oxide film on a test-bar fracture surface was onsite exposed using the FIB technique (Fig. 9). As shown in Fig. 9a, a continuous oxide film was found between the platinum coating layer and the Mg-Al alloy substrate. Fig. 9 (b-c) shows a magnified observation to oxide films, indicating a multi-layered structure (denoted by the red box in Fig. 9c). The bottom layer was enriched with fluorine and oxygen and should be the mixture of fluoride and oxide, which was similar to the "outer layer" shown in Figs. 5 and 7, while the only-oxygen-enriched top layer was similar to the "inner layer" shown in Figs. 5 and 7.

Except the continuous film, some individual particles were also observed in or below the continuous film, as shown in Fig. 9. An Al-enriched particle was detected in the left side of the oxide film shown in Fig. 9b and might be speculated to be spinel Mg_2AlO_4 because it also contains abundant magnesium and oxygen elements. The existing of such Mg_2AlO_4 particles is responsible for the high concentration of aluminium in small areas of the observed film and the uneven distribution of aluminium, as shown in Fig. 5(c). Here it should be emphasized that, although the other part of the bottom layer of the continuous oxide film contains less aluminium than this Al-enriched particle, the Fig. 9c indicated that the amount of aluminium in this bottom layer was still non-negligible, especially when comparing with the outer layer of the film. Below the right side of the oxide film shown in Fig. 9b, a particle was detected and speculated to be MgO because it is rich in Mg and O. According to Wang's result [56], lots of discrete MgO particles can be formed on the surface of the Mg melt by the oxidation of Mg melt and Mg vapor. The MgO particles observed in our present work may be formed due to the same reasons. While, due to the differences in experimental conditions, less Mg melt can be vapored or react with O_2, thus only a few of MgO particles formed in our work. An enrichment of carbon was also found in the film, revealing that CO_2 was able to react with the melt, thus forming carbon or carbides. This carbon concentration was consistent with the relatively high carbon content of the oxide film shown in Table 3 (i.e., the dark region). In the area next to the oxide film.

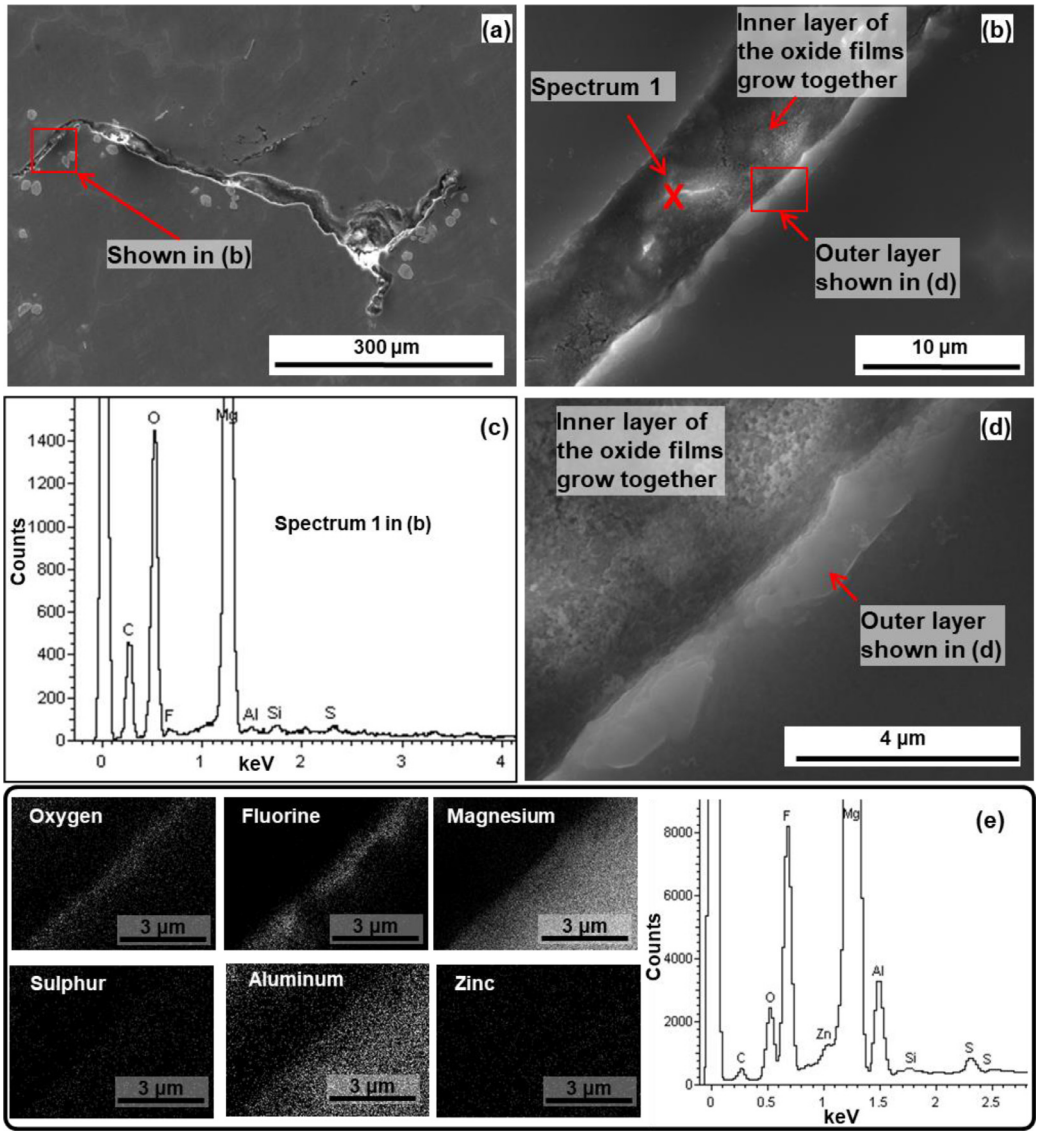

Fig. 7. (a) An example of entrainment defects formed in SF_6/CO_2 and having a multi-layered oxide film, (b) magnified observation of the defect, showing the inner layer of the oxide films has grown together, (c) EDS spectrum of the point denoted in (b), (d) outer layer of the oxide film, (e) SEM-EDS element maps (using Philips JEOL7000) corresponding to the area shown in (d).

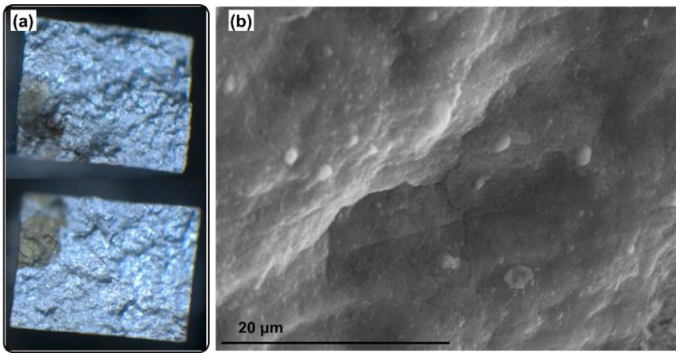

Fig. 8. (a) A pair of the fracture surfaces of a AZ91 alloy tensile test bar, produced in an atmosphere of SF_6/CO_2. The dimension of the fracture surface is 5 mm × 6 mm, (b) surface appearance of the oxide films on the fracture surfaces, showing spots on the film surface.

Table 3
EDS results (wt.%) corresponding to the regions shown in Fig. 8 (cover gas: SF_6/ CO_2).

	C	O	Mg	F	Al	Zn	S	N
Dark region in Fig. 8(a)	7.25	3.64	69.82	3.82	7.03	0.86	-	-
Bright region in Fig. 8(a)	2.10	0.44	82.83	–	13.26	1.36	–	–

This cross-sectional observation of the oxide film on a test bar fracture surface (Fig. 9) further verified the schematic of the entrainment defect shown in Fig. 6(e). The entrainment defects formed in different atmospheres of SF_6/CO_2 and SF_6/air had similar structures, but their compositions were different.

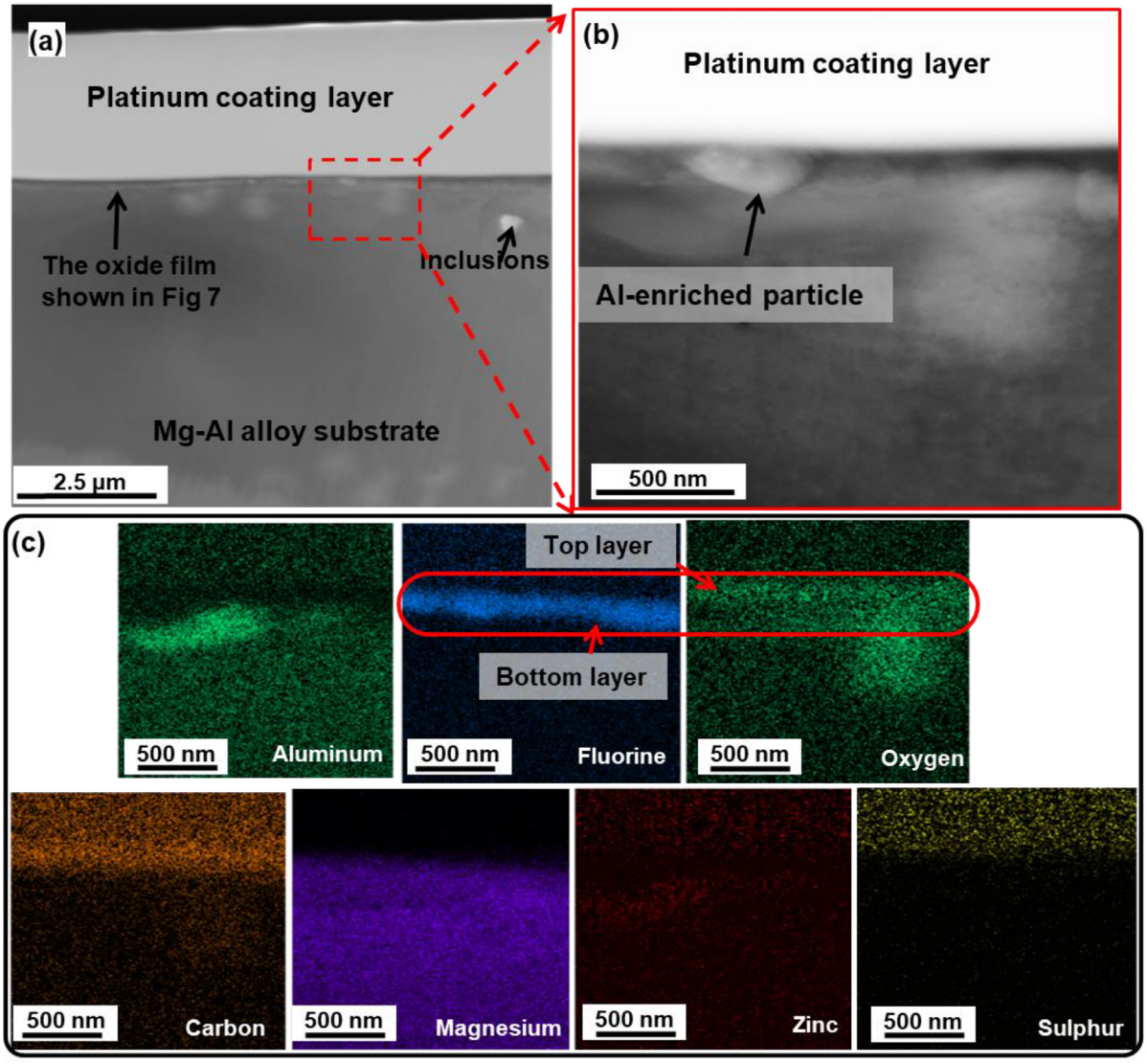

Fig. 9. (a) A cross-sectional observation of the oxide film on the fracture surface of the AZ91 casting produced in SF_6/CO_2, exposed by FIB, (b) a magnified observation of area highlighted in (a), and (c) SEM-EDS elements map of the area shown in (b), obtained by CFEI Quanta 3D FEG FIB-SEM.

3.3. Evolution of the oxide films in the oxidation cell

The results in Section 3.1 and 3.2 have shown the structures and compositions of entrainment defects formed in AZ91 castings under cover gases of SF_6/air and SF_6/CO_2. Different stages of the oxidation reaction may lead to the different structures and compositions of entrainment defects. Although Campbell has conjectured that an entrained gas may react with the surrounding melt, it is rarely reported that the reaction occurring between the Mg-alloy melt and entrapped cover gas. Previous researchers normally focus on the reaction between a Mg-alloy melt and the cover gas in an open environment [38,39,46–52], which was different from the situation of a cover gas trapped into the melt. To further understand the formation of the entrainment defect in an AZ91 alloy, the evolution process of oxide films of the entrainment defect was further studied using an oxidation cell.

Fig. 10 (a and d) shows a surface film held for 5 min in the oxidation cell, protected by 0.5%SF_6/air. There was only one single layer consisting of fluoride and oxide (MgF_2 and MgO). In this surface film. Sulphur was detected in the EDS spectrum, but its amount was too small to be recognized in the element map. The structure and composition of this oxide film was similar to the single-layered films of entrainment defects shown in Fig. 4.

After a holding time of 10 min, a thin (O, S)-enriched top layer (around 700 nm) appeared upon the preliminary F-enriched film, forming a multi-layered structure, as shown in Fig. 10(b and e). The thickness of the (O, S)-enriched top layer increased with increased holding time. As shown in Fig. 10(c and f), the oxide film held for 30 min also had a multi-layered structure, but the thickness of its (O, S)-enriched top layer (around 2.5 μm) was higher than the that of the 10-min oxide film. The multi-layered oxide films shown in

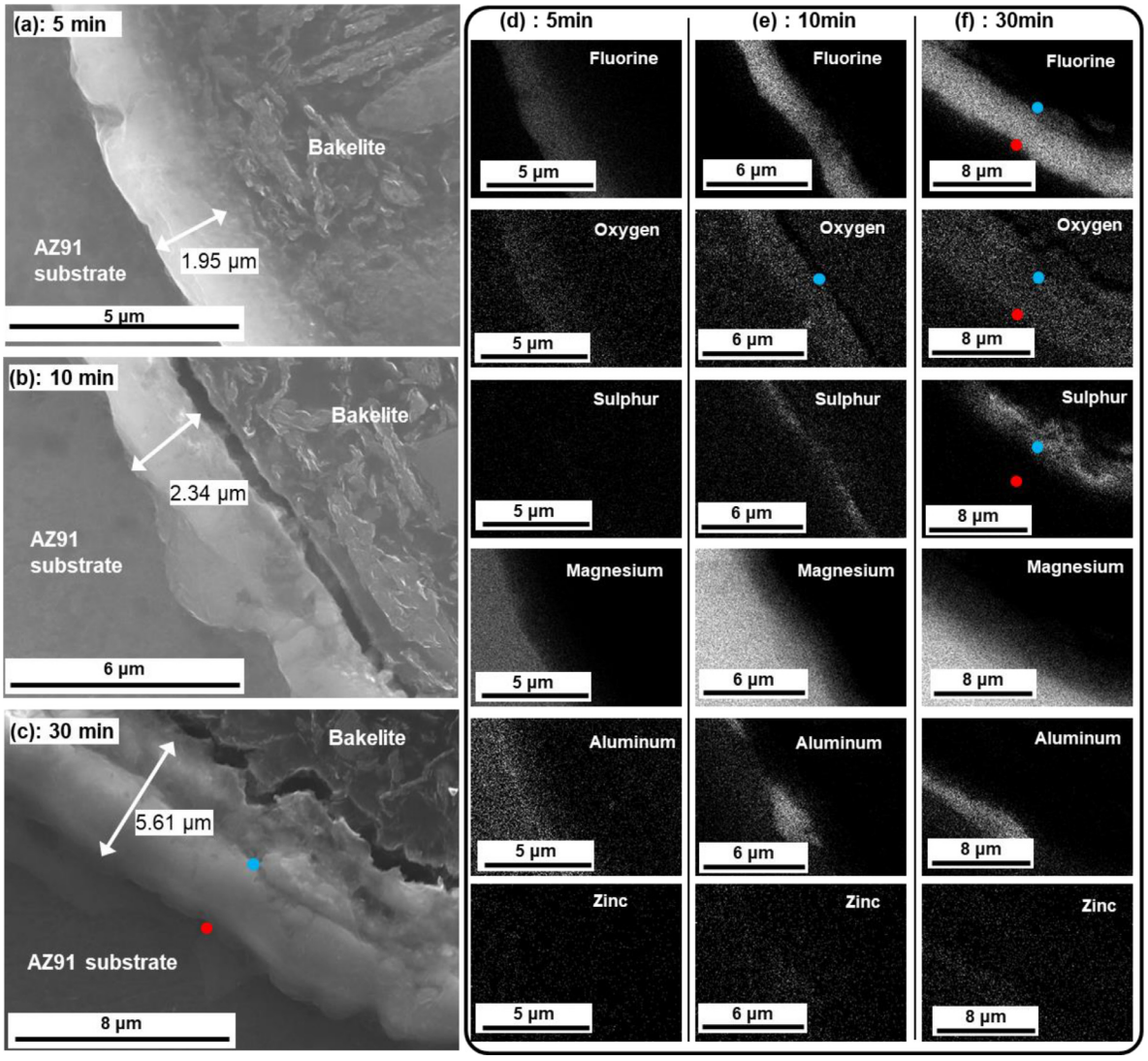

Fig. 10. Oxide films formed in the oxidation cell under a cover gas of 0.5%SF_6/air and held at 700 °C for (a) 5 min; (b) 10 min; (c) 30 min, and (d-f) the SEM-EDS element maps (using Philips JEOL7000) corresponding to the oxide film shown in (a-c) respectively, (d) 5 min; (e) 10 min; (f) 30 min. The red points in (c and f) are the location references, denoting the boundary of the F-enriched layer in different element maps.

Fig. 10(b-c) presented a similar appearance to the films of the sandwich-like defect shown in Fig. 5.

The different structures of the oxide films shown in Fig. 10 indicated that fluorides in the cover gas would be preferentially consumed due to the reaction with the AZ91 alloy melt. After the depletion of fluorides, the residual cover gas reacted further with the liquid AZ91 alloy, forming the top (O, S)-enriched layer in the oxide film. Therefore, the different structures and compositions of entrainment defects shown in Figs. 4 and 5 may be due to an ongoing oxidation reaction between melt and entrapped cover gas.

This multi-layered structure has not been reported in previous publications concerning the protective surface film formed on a Mg-alloy melt [38,46–51]. This may be due to the fact that previous researchers carried out their experiments with an un-limited amount of cover gas, creating a situation where the fluorides in the cover gas were not able to become depleted. Therefore, the oxide film of an entrainment defect had behaviour traits similar to the oxide films shown in Fig. 10, but different from the oxide films formed on the Mg-alloy melt surface reported in [38,46–51].

Similar with the oxide films held in SF_6/air, the oxide films formed in SF_6/CO_2 also had different structures with different holding times in the oxidation cell. Fig. 11(a) shows an oxide film, held on an AZ91 melt surface under a cover gas of 0.5%SF_6/CO_2 for 5 min. This film had a single-layered structure consisting of MgF_2. The existence of MgO could not be confirmed in this film. After the holding time of 30 min, the film had a multi-layered structure; the inner layer was of a compact and uniform appearance and composed of MgF_2, while the outer layer is the mixture of MgF_2 and MgO. Sulphur was not detected in this film, which was different from the surface film formed in 0.5%SF_6/air. Therefore, fluorides in the cover gas of 0.5%SF_6/CO_2 were

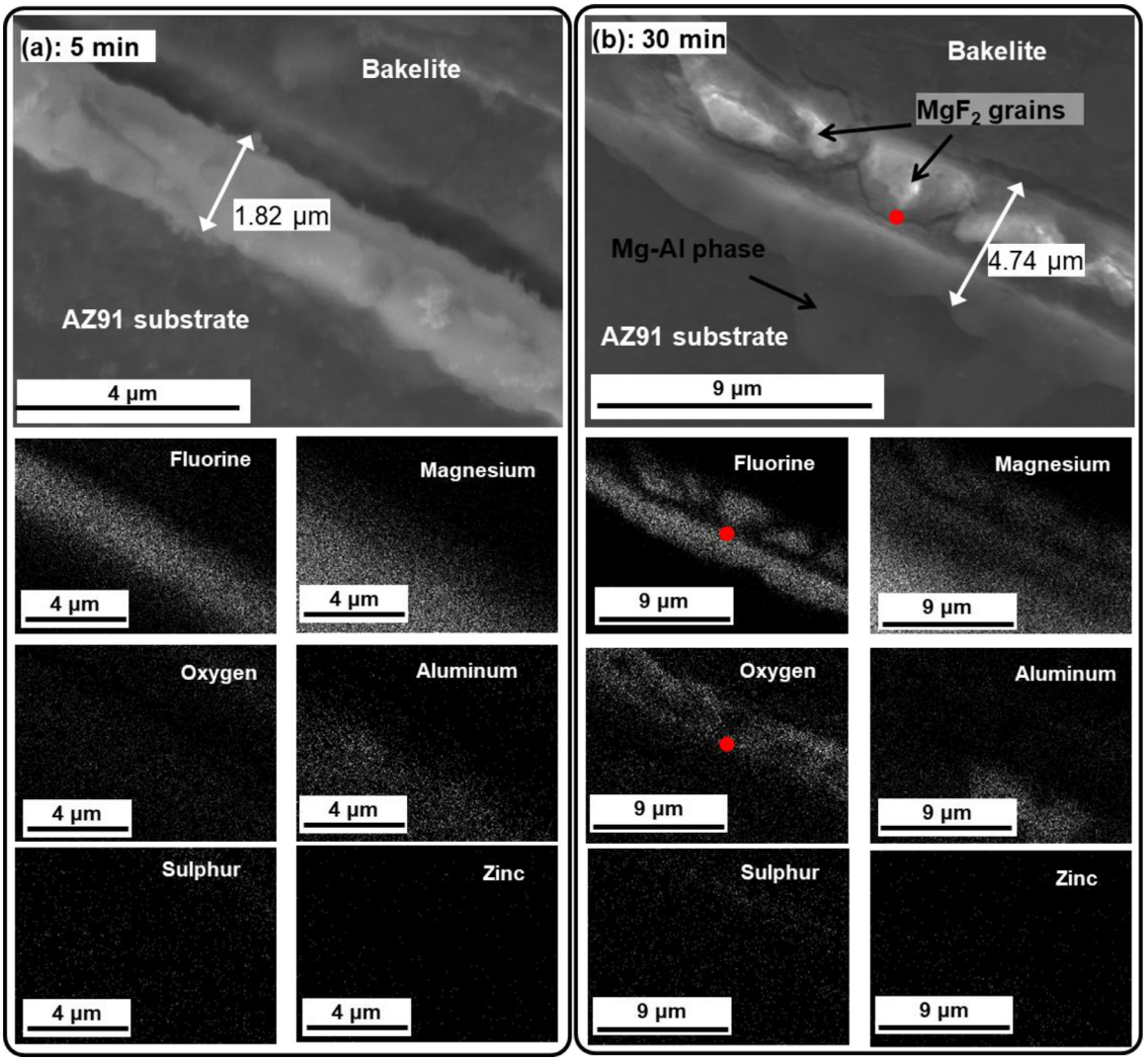

Fig. 11. Oxide films formed in the oxidation cell under a cover gas of 0.5%SF_6/CO_2, and their SEM-EDS element maps (using Philips JEOL7000). They were held at 700 °C for (a) 5 min; (b) 30 min. The red points in (b) are the location references, denoting the boundary between the top and bottom layers in the oxide film.

also preferentially consumed at an early stage of the film growth process. Compared with the film formed in SF_6/air, the MgO in film formed in SF_6/CO_2 appeared later and sulphide did not appear within 30 min. It may mean that the formation and evolution of film in SF_6/air is faster than SF_6/CO_2. CO_2 may have subsequently reacted with the melt to form MgO, while sulphur-containing compounds accumulated in the cover gas and reacted to form sulphide in very late stage (may after 30 min in oxidation cell).

4. Discussion

4.1. Evolution of entrainment defects formed in SF_6/air

HSC software from Outokumpu HSC Chemistry for Windows (http://www.hsc-chemistry.net/) was used to carry out thermodynamic calculations needed to explore the reactions which might occur between the trapped gases and liquid AZ91 alloy. The solutions to the calculations suggest which products are most likely to form in the reaction process between a small amount of cover gas (i.e., the amount within a trapped bubble) and the AZ91-alloy melt.

In the trials, the pressure was set to 1 atm, and the temperature set to 700 °C. The amount of the cover gas was assumed to be 7×10^{-7} kg, with a volume of approximately 0.57 cm^3 (3.14×10^{-8} kmol) for 0.5%SF_6/air, and 0.35 cm^3 (3.12×10^{-8} kmol) for 0.5%SF_6/CO_2. The amount of the AZ91 alloy melt in contact with the trapped gas was assumed to be sufficient to complete all reactions. The decomposition products of SF_6 were SF_5, SF_4, SF_3, SF_2, F_2, S(g), S_2(g) and F(g) [57-60].

Fig. 12 shows the equilibrium diagram of the thermodynamic calculation of the reaction between the AZ91 alloy and 0.5%SF_6/air. In the diagram, the reactants and products with less than 10^{-15} kmol have not been shown, as this was 5 orders of magnitude less than the amount of SF_6 present

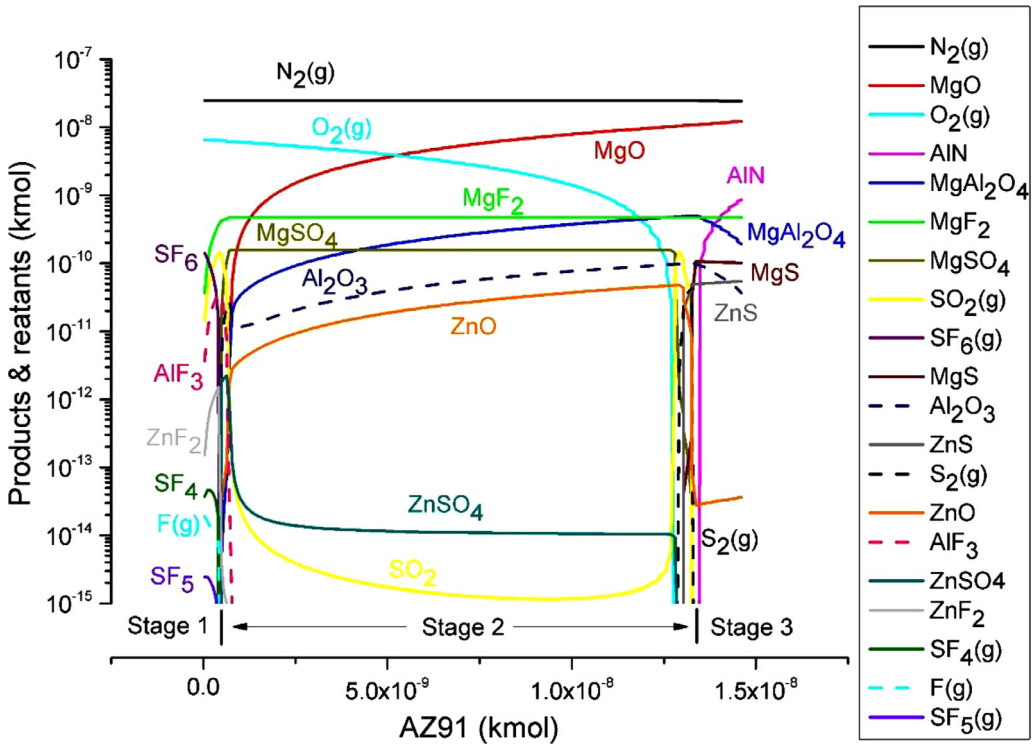

Fig. 12. An equilibrium diagram for the reaction between 7e-7 kg 0.5%SF_6/air and a sufficient amount of AZ91 alloy. The X axis is the amount of AZ91 alloy melt having reacted with the entrained gas, and the vertical Y-axis is the amount of the reactants and products.

($\approx$ 1.57 $\times$ 10^{-10} kmol) and therefore would not affect the observed process in a practical way.

This reaction process could be divided into 3 stages.

Stage 1: The formation of fluorides. the AZ91 melt preferentially reacted with SF_6 and its decomposition products, producing MgF_2, AlF_3, and ZnF_2. However, the amount of ZnF_2 may have been too small to be detected practically (1.25 $\times$ 10^{-12} kmol of ZnF_2 compared with 3 $\times$ 10^{-10} kmol of MgF_2), which may be the reason why Zn was not detected in any the oxide films shown in Sections 3.1–3.3. Meanwhile, sulphur accumulated in the residual gas as SO_2.

Stage 2: The formation of oxides. After the liquid AZ91 alloy had depleted all the available fluorides in the entrapped gas, the amount of AlF_3 and ZnF_2 quickly reduced due to a reaction with Mg. O_2(g) and SO_2 reacted with the AZ91 melt, forming MgO, Al_2O_3, $MgAl_2O_4$, ZnO, $ZnSO_4$ and $MgSO_4$. However, the amount of ZnO and $ZnSO_4$ would have been too small to be found practically by EDS (e.g. 9.5 $\times$ 10^{-12} kmol of ZnO,1.38 $\times$ 10^{-14} kmol of $ZnSO_4$, in contrast to 4.68 $\times$ 10^{-10} kmol of MgF_2, when the amount of AZ91 on the *X*-axis is 2.5 $\times$ 10^{-9} kmol). In the experimental cases, the concentration of F in the cover gas is very low, whole the concentration f O is much higher. Therefore, the stage 1 and 2, i.e, the formation of fluoride and oxide may happen simultaneously at the beginning of the reaction, resulting in the formation of a singer-layered mixture of fluoride and oxide, as shown in Figs. 4 and 10(a). While an inner layer consisted of oxides but fluorides could form after the complete depletion of F element in the cover gas.

Stages 1- 2 theoretically verified the formation process of the multi-layered structure shown in Fig. 10.

The amount of $MgAl_2O_4$ and Al_2O_3 in the oxide film was of a sufficient amount to be detected, which was consistent with the oxide films shown in Fig. 4. However, the existence of aluminium could not be recognized in the oxide films grown in the oxidation cell, as shown in Fig. 10. This absence of Al may be due to the following reactions between the surface film and AZ91 alloy melt:

(1) Al_2O_3 + 3Mg + = 3MgO + 2Al, $\triangle$G(700 °C) = -119.82 kJ/mol
(2) Mg + $MgAl_2O_4$ = MgO + Al, $\triangle$G(700 °C) =-106.34 kJ/mol

which could not be simulated by the HSC software since the thermodynamic calculation was carried out under an assumption that the reactants were in full contact with each other. However, in a practical process, the AZ91 melt and the cover gas would not be able to be in contact with each other completely, due to the existence of the protective surface film.

Stage 3: The formation of Sulphide and nitride. After a holding time of 30 min, the gas-phase fluorides and oxides in the oxidation cell had become depleted, allowing the melt reaction with the residual gas, forming an additional sulphur-enriched layer upon the initial F-enriched or (F, O)-enriched surface film, thus resulting in the observed multi-layered structure shown in Fig. 10 (b and c). Besides, nitrogen reacted with the AZ91 melt until all reactions were

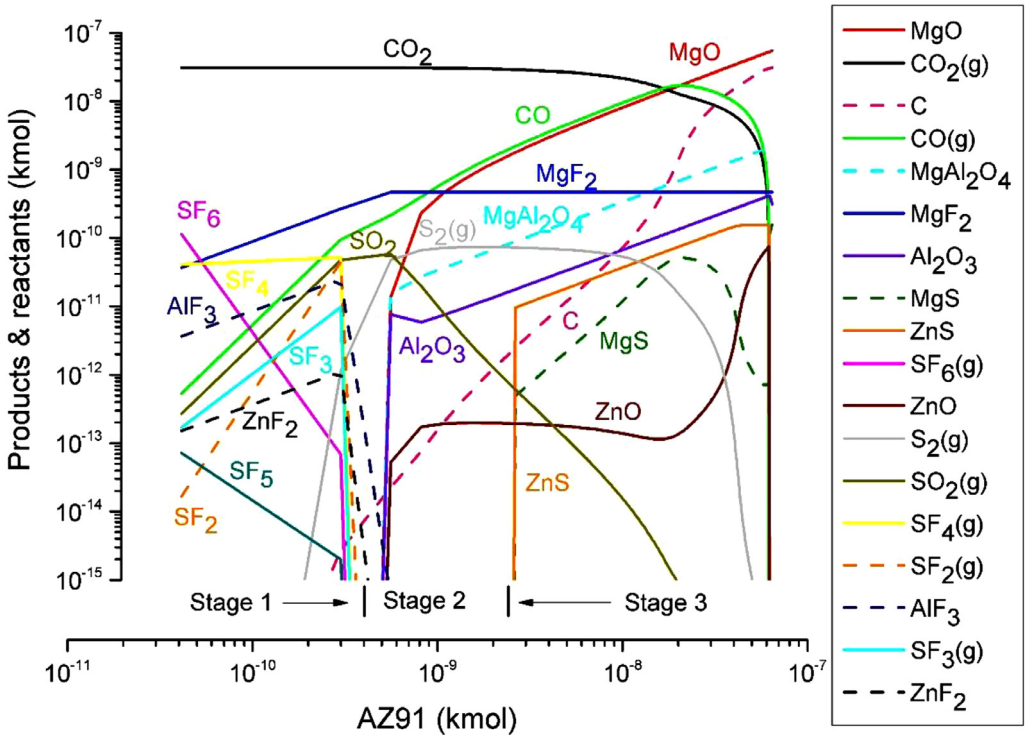

Fig. 13. An equilibrium diagram for the reaction between 7e-7 kg 0.5%SF_6/CO_2 and a sufficient amount of AZ91 alloy. The X axis denotes the amount of Mg alloy melt having reacted with the entrained gas, and the vertical Y-axis denotes the amounts of the reactants and products.

completed. The oxide film shown in Fig. 6 may correspond to this reaction stage due to its nitride content. However, the results shows that the nitrides were not detected in the polished samples shown in Figs. 4 and 5, but only found on the test bar fracture surfaces. The nitrides may have hydrolysed during the sample preparation process, as follows [54]:

(3) $Mg_3N_2 + 6H_2O = 3Mg(OH)_2 + 2NH_3\uparrow$
(4) $AlN + 3H_2O = Al(OH)_3 + NH_3\uparrow$

In addition, Schmidt et al. [61] found that Mg_3N_2 and AlN could react to form ternary nitrides ($Mg_3Al_nN_{n+2}$, n= 1, 2, 3...). HSC software did not contain the database of ternary nitrides, and it could not be added into the calculation. The oxide films in this stage may also contain ternary nitrides.

4.2. Evolution of entrainment defects formed in SF_6/CO_2

Fig. 13 shows the results of the thermodynamic calculation between AZ91 alloy and 0.5%SF_6/CO_2. This reaction processes can also be divided into three stages.

Stage 1: The formation of fluorides. SF_6 and its decomposition products were consumed by the AZ91 melt, forming MgF_2, AlF_3, and ZnF_2. As in the reaction of AZ91 in 0.5%SF_6/air, the amount of ZnF_2 was too small to be detected practically (1.51×10^{-13} kmol of ZnF_2 compared with 2.67×10^{-10} kmol of MgF_2). Sulphur accumulated in the residual trapped gas as S_2(g) and a portion of the S_2(g) reacted with CO_2, to form SO_2 and CO. The products in this reaction stage were consistent with the film shown in Fig. 11(a), which had a single layer structure that contained fluorides only.

Stage 2: The formation of oxides. AlF_3 and ZnF_2 reacted with the Mg in the AZ91 melt, forming MgF_2, Al and Zn. The SO_2 began to be consumed, producing oxides in the surface film and S_2(g) in the cover gas. Meanwhile, the CO_2 directly reacted with the AZ91 melt, forming CO, MgO, ZnO, and Al_2O_3. The oxide films shown in Figs. 9 and 11(b) may correspond to this reaction stage due to their oxygen-enriched layer and multi-layered structure.

The CO in the cover gas could further react with the AZ91 melt, producing C. This carbon may further react with Mg to form Mg carbides, when the temperature reduced (during solidification period) [62]. This may be the reason for the high carbon content in the oxide film shown in Figs. 8-9. Liang et al. [39] also reported carbon-detection in an AZ91 alloy surface film protected by SO_2/CO_2. The produced Al_2O_3 may be further combined with MgO, forming $MgAl_2O_4$ [63]. As discussed in Section 4.1, the alumina and spinel can react with Mg, causing an absence of aluminium in the surface films, as shown in Fig. 11.

Stage 3: The formation of Sulphide. the AZ91 melt began to consume S_2(g) in the residual entrapped gas, forming ZnS and MgS. These reactions did not occur until the last stage of the reaction process, which could be the reason why the S-content in the defect shown Fig. 7(c) was small.

In summary, thermodynamic calculations indicate that the AZ91 melt will react with the cover gas to form fluorides

firstly, then oxides and sulphides in the last. The oxide film in the different reaction stages would have different structures and compositions.

4.3. Effect of the carrier gases on consumption of the entrained gas and the reproducibility of AZ91 castings

The evolution processes of entrainment defects, formed in SF_6/air and SF_6/CO_2, have been suggested in Sections 4.1 and 4.2. The theoretical calculations were verified with respect to the corresponding oxide films found in practical samples. The atmosphere within an entrainment defect could be efficiently consumed due to the reaction with liquid Mg-alloy, in a scenario dissimilar to the Al-alloy system (i.e., nitrogen in an entrained air bubble would not efficiently react with Al-alloy melt [64,65], however, nitrogen would be more readily consumed in liquid Mg alloys, commonly referred to as "nitrogen burning" [66]).

The reaction between the entrained gas and the surrounding liquid Mg-alloy converted the entrained gas into solid compounds (e.g. MgO) within the oxide film, thus reducing the void volume of the entrainment defect and hence probably causing a collapse of the defect (e.g., if an entrained gas of air was depleted by the surrounding liquid Mg-alloy, under an assumption that the melt temperature is 700 °C and the depth of liquid Mg-alloy is 10 cm, the total volume of the final solid products would be 0.044% of the initial volume taken by the entrapped air).

The relationship between the void volume reduction of entrainment defects and the corresponding casting properties has been widely studied in Al-alloy castings. Nyahumwa and Campbell [16] reported that the Hot Isostatic Pressing (HIP) process caused the entrainment defects in Al-alloy castings to collapse and their oxide surfaces forced into contact. The fatigue lives of their castings were improved after HIP. Nyahumwa and Campbell [16] also suggested a potential bonding of the double oxide films that were in contact with each other, but there was no direct evidence to support this. This binding phenomenon was further investigated by Aryafar et.al.[8], who re-melted two Al-alloy bars with oxide skins in a steel tube and then carried out a tensile strength test on the solidified sample. They found that the oxide skins of the Al-alloy bars strongly bonded with each other and became even stronger with an extension of the melt holding time, indicating a potential "healing" phenomenon due to the consumption of the entrained gas within the double oxide film structure. In addition, Raidszadeh and Griffiths [9,19] successfully reduced the negative effect of entrainment defects on the reproducibility of Al-alloy castings, by extending the melt holding time before solidification, which allowed the entrained gas to have a longer time to react with the surrounding melt.

With consideration of the previous work mentioned, the consumption of the entrained gas in Mg-alloy castings may diminish the negative effect of entrainment defects in the following two ways.

(1) *Bonding phenomenon of the double oxide films*. The sandwich-like structure shown in Fig. 5 and 7 indicated a potential bonding of the double oxide film structure. However, more evidence is required to quantify the increase in strength due to the bonding of the oxide films.

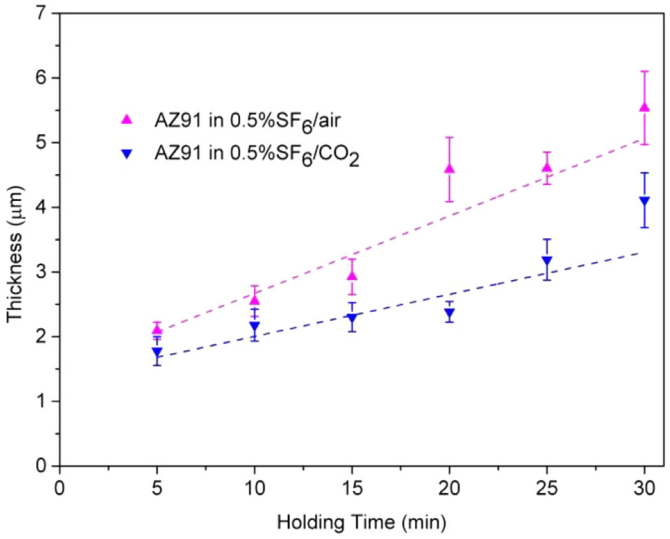

Fig. 14. A comparison of the AZ91 alloy oxide film growth rates in 0.5%SF_6/air and 0.5%SF_6/CO_2

(2) V*oid volume reduction of entrainment defects*. The positive effect of void-volume reduction on the quality of castings has been widely demonstrated by the HIP process [67]. As the evolution processes discussed in Section 4.1–4.2, the oxide films of entrainment defects can grow together due to an ongoing reaction between the entrained gas and surrounding AZ91 alloy melt. The volume of the final solid products was significant small compared with the entrained gas (i.e., 0.044% as previously mentioned).

Therefore, the consumption rate of the entrained gas (i.e., the growth rate of oxide films) may be a critical parameter for improving the quality of AZ91 alloy castings. The oxide film growth rate in the oxidization cell was accordingly further investigated.

Fig. 14 shows a comparison of the surface film growth rates in different cover gases (i.e., 0.5%SF_6/air and 0.5%SF_6/CO_2). 15 random points on each sample were selected for film thickness measurements. The 95% confidence interval (95%CI) was computed under an assumption that the variation of the film thickness followed a Gaussian distribution. It can be seen that all the surface films formed in 0.5%SF_6/air grew faster than those formed in 0.5%SF_6/CO_2. The different growth rates suggested that the entrained-gas consumption rate of 0.5%SF_6/air was higher than that of 0.5%SF_6/CO_2, which was more beneficial for the consumption of the entrained gas.

It should be noted that, in the oxidation cell, the contact area of liquid AZ91 alloy and cover gas (i.e. the size of the crucible) was relatively small with consideration of the large volume of melt and gas. Consequently, the holding time for the oxide film growth within the oxidation cell was comparatively long (i.e., 5–30 min). However, the entrainment defects contained in a real casting are comparatively very small (i.e.,

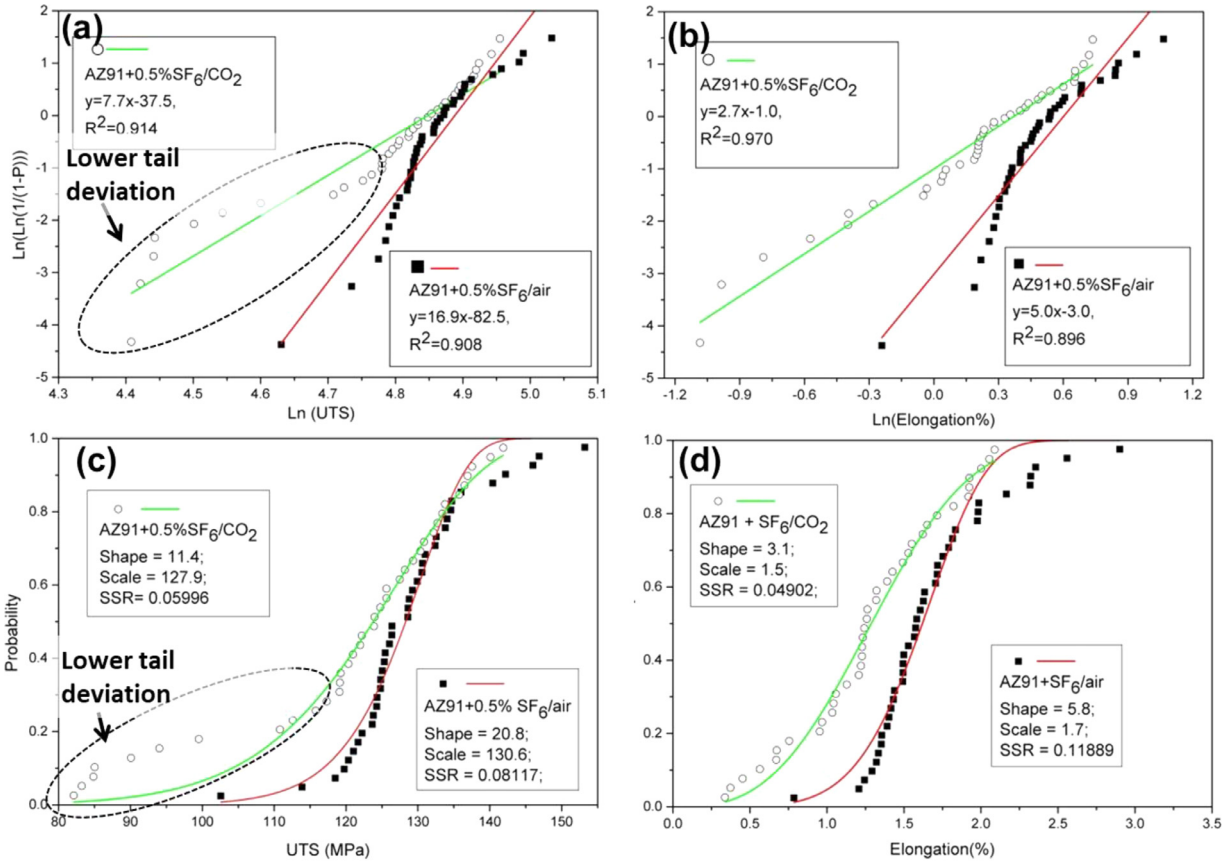

Fig. 15. The Weibull modulus of AZ91 castings produced in different atmospheres, estimated by (a-b) the linear least square method, (c-d) the non-linear least square method, where SSR is the sum of residual squares.

a few microns size as shown in Figs. 3–6, and [7]), and the entrained gas is fully enclosed by the surrounding melt, creating a relatively large contact area. Hence the reaction time for cover gas and the AZ91 alloy melt may be comparatively short. In addition, the solidification time of real Mg-alloy sand castings can be a few minutes (e.g. Guo [68] reported that a Mg-alloy sand casting with 60 mm diameter required 4 min to be solidified). Therefore, it can be expected that an entrained gas trapped during an Mg-alloy melt pouring process will be readily consumed by the surrounding melt, especially for sand castings and large-size castings, where solidification times are long.

Therefore, the different cover gases (0.5%SF_6/air and 0.5%SF_6/CO_2) associated with different consumption rates of the entrained gases may affect the reproducibility of the final castings. To verify this assumption, the AZ91 castings produced in 0.5%SF_6/air and 0.5%SF_6/CO_2 were machined into test bars for mechanical evaluation. A Weibull analysis was carried out using both linear least square (LLS) method and non-linear least square (non-LLS) method [69].

Fig. 15(a-b) shows a traditional 2-p linearized Weibull plot of the UTS and elongation of the AZ91 alloy castings, obtained by the LLS method. The estimator used is P= (i-0.5)/N, which was suggested to cause the lowest bias among all the popular estimators [69,70]. The casting produced in SF_6/air has an UTS Weibull moduli of 16.9, and an elongation Weibull moduli of 5.0. In contrast, the UTS and elongation Weibull modulus of the casting produced in SF_6/CO_2 are 7.7 and 2.7 respectively, suggesting that the reproducibility of the casting protected by SF_6/CO_2 were much lower than that produced in SF_6/air.

In addition, the author's previous publication [69] demonstrated a shortcoming of the linearized Weibull plots, which may cause a higher bias and incorrect R^2 interruption of the Weibull estimation. A Non-LLS Weibull estimation was therefore carried out, as shown in Fig. 15 (c-d). The UTS Weibull modulus of the SF_6/air casting was 20.8, while the casting produced under SF_6/CO_2 had a lower UTS Weibull modulus of 11.4, showing a clear difference in their reproducibility. In addition, the SF_6/air elongation (El%) dataset also had a Weibull modulus (shape = 5.8) higher than the elongation dataset of SF_6/CO_2 (shape = 3.1). Therefore, both the LLS and Non-LLS estimations suggested that the SF_6/air casting has a higher reproducibility than the SF_6/CO_2 casting. It supports the method that the use of air instead of CO_2 contributes to a quicker consumption of the entrained gas, which may reduce the void volume within the defects. Therefore, the use of 0.5%SF_6/air instead of 0.5%SF_6/CO_2 (which increased the consumption rate of the entrained gas) improved the reproducibility of the AZ91 castings.

However, it should be noted that not all the Mg-alloy foundries followed the casting process used in present work. The Mg-alloy melt in present work was degassed, thus reducing the effect of hydrogen on the consumption of the entrained gas (i.e., hydrogen could diffuse into the entrained gas, potentially suppressing the depletion of the entrained gas [7,71,72]). In contrast, in Mg-alloy foundries, the Mg-alloy melt is not normally degassed, since it was widely believed that there is not a 'gas problem' when casting magnesium and hence no significant change in tensile properties [73]. Although studies have shown the negative effect of hydrogen on the mechanical properties of Mg-alloy castings [41,42,73], a degassing process is still not very popular in Mg-alloy foundries.

Moreover, in present work, the sand mould cavity was flushed with the SF_6 cover gas prior to pouring [22]. However, not all the Mg-alloy foundries flushed the mould cavity in this way. For example, the Stone Foundry Ltd (UK) used sulphur powder instead of the cover-gas flushing. The entrained gas within their castings may be SO_2/air, rather than the protective gas.

Therefore, although the results in present work have shown that using air instead of CO_2 improved the reproducibility of the final casting, it still requires further investigations to confirm the effect of carrier gases with respect to different industrial Mg-alloy casting processes.

7. Conclusion

1. Entrainment defects formed in an AZ91 alloy were observed. Their oxide films had two types of structure: single-layered and multi-layered. The multi-layered oxide film can grow together forming a sandwich-like structure in the final casting.
2. Both the experimental results and the theoretical thermodynamic calculations demonstrated that fluorides in the trapped gas were depleted prior to the consumption of sulphur. A three-stage evolution process of the double oxide film defects has been suggested. The oxide films contained different combinations of compounds, depending on the evolution stage. The defects formed in SF_6/air had a similar structure to those formed in SF_6/CO_2, but the compositions of their oxide films were different. The oxide-film formation and evolution process of the entrainment defects were different from that of the Mg-alloy surface films previous reported (i.e., MgO formed prior to MgF_2).
3. The growth rate of the oxide film was demonstrated to be greater under SF_6/air than SF_6/CO_2, contributing to a quicker consumption of the damaging entrapped gas. The reproducibility of an AZ91 alloy casting improved when using SF_6/air instead of SF_6/CO_2.

Acknowledgements

The authors acknowledge funding from the EPSRC LiME grant EP/H026177/1, and the help from Dr W.D. Griffiths and Mr. Adrian Carden (University of Birmingham). The casting work was carried out in University of Birmingham.

Reference

[1] M.K. McNutt, SALAZAR K., Magnesium, Compounds & Metal, U.S. Geological Survey and U.S. Department of the Interior, Reston, Virginia, 2013.
[2] MagnesiumCompounds & Metal, U.S. Geological Survey and U.S. Department of the Interior, 1996.
[3] I. Ostrovsky, Y. Henn, in: ASTEC'07 International Conference-New Challenges in Aeronautics, Moscow, 2007, pp. 1–5. Aug 19-22.
[4] Y. Wan, B. Tang, Y. Gao, L. Tang, G. Sha, B. Zhang, N. Liang, C. Liu, S. Jiang, Z. Chen, X. Guo, Y. Zhao, Acta Mater. 200 (2020) 274–286.
[5] J.T.J. Burd, E.A. Moore, H. Ezzat, R. Kirchain, R. Roth, Appl. Energy 283 (2021) 116269.
[6] A.M. Lewis, J.C. Kelly, G.A. Keoleian, Appl. Energy 126 (2014) 13–20.
[7] J. Campbell, Castings, Butterworth-Heinemann, Oxford, 2004.
[8] M. Aryafar, R. Raiszadeh, A. Shalbafzadeh, J. Mater. Sci. 45 (2010) 3041–3051.
[9] R. Raiszadeh, W.D. Griffiths, Metall. Mater. Trans. B-Process Metall. Mater. Process. Sci. 42 (2011) 133–143.
[10] R. Raiszadeh, W.D. Griffiths, J. Alloy. Compd. 491 (2010) 575–580.
[11] L. Peng, G. Zeng, T.C. Su, H. Yasuda, K. Nogita, C.M. Gourlay, JOM 71 (2019) 2235–2244.
[12] S. Ganguly, A.K. Mondal, S. Sarkar, A. Basu, S. Kumar, C. Blawert, Corros. Sci. 166 (2020).
[13] G.E. Bozchaloei, N. Varahram, P. Davami, S.K. Kim, Mater. Sci. Eng. A-Struct. Mater. Prop. Microstruct. Process. 548 (2012) 99–105.
[14] S. Fox, J. Campbell, Scr. Mater. 43 (2000) 881–886.
[15] M. Cox, R.A. Harding, J. Campbell, Mater. Sci. Technol. 19 (2003) 613–625.
[16] C. Nyahumwa, N.R. Green, J. Campbell, Metall. Mater. Trans. A-Phys. Metall. Mater. Sci. 32 (2001) 349–358.
[17] A. Ardekhani, R. Raiszadeh, J. Mater. Eng. Perform. 21 (2012) 1352–1362.
[18] X. Dai, X. Yang, J. Campbell, J. Wood, Mater. Sci. Technol. 20 (2004) 505–513.
[19] E.M. Elgallad, M.F. Ibrahim, H.W. Doty, F.H. Samuel, Philos. Mag. 98 (2018) 1337–1359.
[20] W.D. Griffiths, N.W. Lai, Metall. Mater. Trans. A-Phys. Metall. Mater. Sci. 38A (2007) 190–196.
[21] A.R. Mirak, M. Divandari, S.M.A. Boutorabi, J. Campbell, Int. J. Cast Met. Res. 20 (2007) 215–220.
[22] C. Cingi, Laboratory of Foundry Engineering, Helsinki University of Technology, Espoo, Finland, 2006.
[23] Y. Jia, J. Hou, H. Wang, Q. Le, Q. Lan, X. Chen, L. Bao, J. Mater. Process. Technol. 278 (2020) 116542.
[24] S. Ouyang, G. Yang, H. Qin, S. Luo, L. Xiao, W. Jie, Mater. Sci. Eng. A 780 (2020) 139138.
[25] S.-m. Xiong, X.-F. Wang, Trans. Nonferrous Met. Soc. China 20 (2010) 1228–1234.
[26] G.V. ResearchGrand View Research, 2018 USA.
[27] T. Li, J. Davies, Metall. Mater. Trans. A 51 (2020) 5389–5400.
[28] J.F. Fruehling, The University of Michigan, 1970.
[29] S. Couling, in: 36th Annual World Conference on Magnesium, Norway, 1979, pp. 54–57.
[30] S. Cashion, N. Ricketts, P. Hayes, J. Light Met. 2 (2002) 43–47.
[31] S. Cashion, N. Ricketts, P. Hayes, J. Light Met. 2 (2002) 37–42.
[32] K. Aarstad, G. Tranell, G. Pettersen, T.A. Engh, Various Techniques to Study the Surface of Magnesium Protected by SF6, TMS, 2003.
[33] S.-M. Xiong, X.-L. Liu, Metall. Mater. Trans. A 38 (2007) 428–434.
[34] T.-S. Shih, J.-B. Liu, P.-S. Wei, Mater. Chem. Phys. 104 (2007) 497–504.
[35] G. Pettersen, E. Øvrelid, G. Tranell, J. Fenstad, H. Gjestland, Mater. Sci. Eng. A 332 (2002) 285–294.
[36] H. Bo, L.B. Liu, Z.P. Jin, J. Alloy. Compd. 490 (2010) 318–325.
[37] A. Mirak, C. Davidson, J. Taylor, Corros. Sci. 52 (2010) 1992–2000.
[38] B.D. Lee, U.H. Beak, K.W. Lee, G.S. Han, J.W. Han, Mater. Trans. 54 (2013) 66–73.

[39] W.Z. Liang, Q. Gao, F. Chen, H.H. Liu, Z.H. Zhao, China Foundry 9 (2012) 226–230.
[40] U.I. Gol'dshleger, E.Y. Shafirovich, Combust. Explos. Shock Waves 35 (1999) 637–644.
[41] A. Elsayed, S.L. Sin, E. Vandersluis, J. Hill, S. Ahmad, C. Ravindran, S. Amer Foundry, Trans. Am. Foundry Soc. 120 (2012) 423–429.
[42] E. Zhang, G.J. Wang, Z.C. Hu, Mater. Sci. Technol. 26 (2010) 1253–1258.
[43] N.R. Green, J. Campbell, Mater. Sci. Eng. A-Struct. Mater. Prop. Microstruct. Process. 173 (1993) 261–266.
[44] C Reilly, MR Jolly, NR Green, in: Proceedings of MCWASP XII - 12th Modelling of Casting, Welding and Advanced Solidifcation Processes, Vancouver, Canada, 2009.
[45] H.E. Friedrich, B.L. Mordike, Springer, Germany, 2006.
[46] C. Zheng, B.R. Qin, X.B. Lou, in: Proceedings of the 2010 International Conference on Mechanical, Industrial, and Manufacturing Technologies, ASME, 2010, pp. 383–388. Mimt 2010.
[47] S.M. Xiong, X.F. Wang, Trans. Nonferrous Met. Soc. China 20 (2010) 1228–1234.
[48] S.M. Xiong, X.L. Liu, Metall. Mater. Trans. A-Phys. Metall. Mater. Sci. 38A (2007) 428–434.
[49] T.S. Shih, J.B. Liu, P.S. Wei, Mater. Chem. Phys. 104 (2007) 497–504.
[50] K. Aarstad, G. Tranell, G. Pettersen, T.A. Engh, Magn. Technol. (2003) 5–10.
[51] G. Pettersen, E. Ovrelid, G. Tranell, J. Fenstad, H. Gjestland, Mater. Sci. Eng. A-Struct. Mater. Prop. Microstruct. Process. 332 (2002) 285–294.
[52] X.F. Wang, S.M. Xiong, Corros. Sci. 66 (2013) 300–307.
[53] S.H. Nie, S.M. Xiong, B.C. Liu, Mater. Sci. Eng. A-Struct. Mater. Prop. Microstruct. Process. 422 (2006) 346–351.
[54] C. Bauer, A. Mogessie, U. Galovsky, Zeitschrift Fur Metallkunde 97 (2006) 164–168.
[55] Q.G. Wang, D. Apelian, D.A. Lados, J. Light Met. 1 (2001) 73–84.
[56] S. Wang, Y. Wang, Q. Ramasse, Z. Fan, Metall. Mater. Trans. A 51 (2020) 2957–2974.
[57] S. Hayashi, W. Minami, T. Oguchi, H.J. Kim, Kag. Kog. Ronbunshu 35 (2009) 411–415.
[58] K. Aarstad, Norwegian University of Science and Technology, 2004.
[59] R.L. Wilkins, J. Chem. Phys. 51 (1969) 853 -&.
[60] O. Kubaschewski, K. Hesselemam, Thermo-Chemical Properties of Inorganic Substances, Springer-Verlag, Belin, 1991.
[61] R. Schmidt, M. Strobele, K. Eichele, H.J. Meyer, Eur. J. Inorg. Chem. (2017) 2727–2735.
[62] B. Hu, Y. Du, H. Xu, W. Sun, W.W. Zhang, D. Zhao, J. Min. Metall. Sect. B-Metall. 46 (2010) 97–103.
[63] O. Salas, H. Ni, V. Jayaram, K.C. Vlach, C.G. Levi, R. Mehrabian, J. Mater. Res. 6 (1991) 1964–1981.
[64] S.S.S. Kumari, U.T.S. Pillai, B.C. Pai, J. Alloy. Compd. 509 (2011) 2503–2509.
[65] H. Scholz, P. Greil, J. Mater. Sci. 26 (1991) 669–677.
[66] P. Biedenkopf, A. Karger, M. Laukotter, W. Schneider, Magn. Technol. 2005 (2005) 39–42.
[67] H.V. Atkinson, S. Davies, Metall. Mater. Trans. A 31 (2000) 2981–3000.
[68] E.J. Guo, L. Wang, Y.C. Feng, L.P. Wang, Y.H. Chen, J. Therm. Anal. Calorim. 135 (2019) 2001–2008.
[69] T. Li, W.D. Griffiths, J. Chen, Metall. Mater. Trans. A-Phys. Metall. Mater. Sci. 48A (2017) 5516–5528.
[70] M. Tiryakioglu, D. Hudak, J. Mater. Sci. 42 (2007) 10173–10179.
[71] Y. Yue, W.D. Griffiths, J.L. Fife, N.R. Green, in: Proceedings of the 1st International Conference on 3d Materials Science, 2012, pp. 131–136.
[72] R. Raiszadeh, W.D. Griffiths, Metall. Mater. Trans. B-Process Metall. Mater. Process. Sci. 37 (2006) 865–871.
[73] Z.C. Hu, E.L. Zhang, S.Y. Zeng, Mater. Sci. Technol. 24 (2008) 1304–1308.